Surfaces and Interfaces 46 (2024) 104078

Contents lists available at ScienceDirect

Surfaces and Interfaces

journal homepage: www.sciencedirect.com/journal/surfaces-and-interfaces

Efficient solar-to-hydrogen conversion based on synergetic effects between Pd clusters and CdS nanoparticles supported on a sulfur-functionalized graphene

María L. Godino-Salido [a,*], Alba M. Valbuena-Rus [a], María D. Gutiérrez-Valero [a], Victor K. Abdelkader-Fernández [b], Rubén Cruz-Sánchez [a], F. Javier López-Garzón [b], Manuel Melguizo [a], Rafael López-Garzón [a]

[a] Department of Inorganic and Organic Chemistry, Faculty of Experimental Sciences, University of Jaén, 23071, Jaén, Spain
[b] Department of Inorganic Chemistry, Faculty of Sciences, University of Granada, 18071, Granada, Spain

ARTICLE INFO

Keywords:
Pd-clusters
Sulfur-functionalized graphene
Cadmium sulfide
Solar photocatalysis
Solar hydrogen photogeneration

ABSTRACT

A new hybrid, GSw-Pd-CdS, consisting of CdS nanoparticles and Pd clusters supported on S-functionalized graphene, GSw, has been obtained for photocatalytic water reduction. GSw has been prepared by mild treatment of graphene, G, with cold CS_2 plasma allowing the G sp^2 moieties to be preserved. GSw-Pd-CdS was prepared under mild conditions by the sequential adsorption on GSw of small-size Pd particles followed by the slow precipitation of CdS. The support of Pd clusters on GSw is controlled by the interaction with S-functions. The support of the CdS nanoparticles occurred by the physical adsorption on GSw. The GSw-Pd-CdS hybrid shows high photocatalytic activity in water reduction providing a constant average H_2 production of 3.79 mmol g^{-1} h^{-1} during 20 h. This value outperforms 31.1 times that of CdS. The excellent behavior of the hybrid is based on suitable optical properties of Pd clusters and on the preservation of the graphene π-conjugated moieties act as active reduction sites. The analysis of both the structure and the optical properties of GSw-Pd-CdS and its components allowed to propose a reliable mechanism to the photocatalytic reduction in which the Pd clusters and the GSw cocatalysts act as hole receptor and electron receptor from CdS, respectively.

1. Introduction

The social concern about the global warming is speeding up as the effects of the climate change are becoming more and more evident. This is driving extensive demand for renewable energy sources to reduce the emissions of greenhouse gases from fossil fuels, which nowadays are the main source of energy. This is boosting extensive research in developing technologies based on the use of renewable sources [1,2]. The sun is an endless source of energy (in the time scale of the human beings) that even though it is difficult to be directly handled, it can be converted into another energy sources including chemical sources as hydrogen. Hydrogen, is a chemical fuel that can be obtained from water and whose combustion with oxygen produces water as the only reaction product. Moreover, it can be also used in fuel cells to produce energy and in many industrial reactions.

The water splitting can be addressed by using semiconductor materials whose activation with sunlight as energy source results in the formation of electron-positive hole pairs capable of inducing the redox decomposition of water. This is accomplished if the semiconducting material conduction band (CB) is more negative than 0.00 eV and the valence band (VB) more positive than 1.23 eV [3]. Nevertheless, in practice, the required band gap is larger than 1.23 eV due to the over-potential derived from the kinetic barriers in each process (mainly in case of oxygen oxidation). Moreover, an important limitation for the efficient conversion of light into hydrogen and oxygen through the above process, comes from the trend of the generated electron-hole pairs to recombine. Thus, the new materials for the total or partial O_2 or H_2 production by photocatalytic water splitting require on the one hand optical and electronic properties of the semiconductor phase. On the other, the electron-hole recombination needs to be at least partially prevented. These requirements can be accomplished (among other strategies) by hybridizing the semiconductor with suitable cocatalysts.

* Corresponding author.
E-mail address: mlgodino@ujaen.es (M.L. Godino-Salido).

https://doi.org/10.1016/j.surfin.2024.104078
Received 13 December 2023; Received in revised form 31 January 2024; Accepted 16 February 2024
Available online 18 February 2024

It has been reported a wide range of metal-based semiconductors, including sulfides, nitrides, single metal oxydes and double metal oxydes (perovskites) that have been successfully used in water reduction reaction [4–6]. Among them a great interest has been focussed in CdS [4,7–9]. This is mainly due to this semiconductor fits suitable optical properties to be activated by visible light, i. e. a band gap of c.a. 2.4 eV, and suitable CB position to proton reduction [10,11]. An additional advantage is that it can be obtained as ultrathin layers [12,13] which help the charge carriers to reach more easily the surface of the catalyst. The thickness control of CdS crystals (which can be achieved by several ways) also allows some control on its behavior and semiconductor character, as the band gap of the crystals increases as the thickness decreases [14–16]. In spite of this, the efficiency of these strategies is quite limited due to electron-hole recombination is fast. A successful strategy to improve its photocatalytic efficiency consists in combining CdS with suitable 2D semiconductors capable to accept electrons from the former to the surface of the second, which stabilizes the charge separation [7,17,18].

We have reported [19] that the photocatalytic activity of CdS in water reduction is very significantly increased when it is hybridized. In particular, a hybrid consisting of CdS, a polyamine-functionalized graphene and PdS shows notable results in this reaction. The role of the hybrid components on the water reduction is discussed in the paper [19]. In spite of the excellent performance of this hybrid in water reduction, it was found that the aliphatic polyamine functions attached to Cπ centres of the graphene (G) layers favour extended stacking of the functionalized G sheets via hydrogen bonding formation of the –N-H·····N– type, between amino functions attached to the surface of adjacent sheets. It is believed that this fact results in shielding effect making difficult the light to reach the inner active CdS centres, which probably limits its photocatalytic efficiency [7]. Experimental results supporting the stacking of polyamine functionalized G layers were, i) the acid-base properties of the polyamine attached to the sheets suffers significant changes relative to the free polyamine [19], indicating that the stacking of sheets probably remain in water solution, ii) a sharp decrease of the BET surface of G (468.0 $m^2\ g^{-1}$) under adsorption of the polyamine derivative (101.9 $m^2\ g^{-1}$ for the polyamine functionalized G) [19], i.e. the stacking of the polyamine functionalized G sheets results in decrease of the mesopore surface (which mainly contributes to the BET surface). Even when functionalized graphene with other similar polyamine functionalities is used, in addition to observing similar stacking of the functionalized G, adsorption of metal ions as $PdCl_4^{2-}$ does not affect the stacked structure, i.e. most of the metal ions remain in the very narrow pores between the stacked sheets [20]. With this background in mind, in this work we have considered interesting the design of a new G-based photocatalyst that pays attention, among others, to this point.

A new hybrid based on CdS + graphene has been prepared, using a sulfur-functionalized graphene as support (GSw), which has been obtained by CS_2 cold plasma treatment of the graphene (G) used in reference 19, as previously reported [21]. The resulting GSw contains mainly C–S–C and C–S–H functions and small amounts of C-SO-C and C-SO_2-C which are attached to the edges of the graphene sheets. The BET surface area of GSw (430.0 $m^2\ g^{-1}$) [21] is very similar to that of the precursor G (468.0 $m^2\ g^{-1}$, see above) which points out that (probably due to coplanarity of S-functionalities with G-sheets) in this case the possible interactions between sheets dont take place via stacking. Thus, the role of GSw in this new CdS-based hybrid is twofold. On the one hand, the sulfur containing functions seems not to induce additional stacking to that of G [19–22]. On the other, the sulfur containing groups are able to capture palladium from solution due to the high affinity of sulfur functions (soft Lewis bases) to palladium (soft Lewis acid). This results in palladium deposition on the graphene surface forming size-homogeneous S-Pd nanoclusters and Pd nanoparticles [23,24]. Both nanostructures show interesting optical properties as they absorb light in a wide wavelength range which covers both UV–Vis and NIR ranges [24–26] which ensures efficient light harvesting. Thus, it is expected these nanostructures act as efficient cocatalyst when they combine with CdS on the surface of GSw.

This paper reports the preparation, characterization and photocatalytic activity in water reduction of the GSw-Pd-CdS hybrid. This material has been obtained by deposition of CdS and Pd on the surface of the sulfur-functionalized graphene, GSw. The photocatalytic activity in water reduction of the hybrid is compared with those of GSw-Pd, Pd-CdS and CdS materials and the mechanisms of the reaction are discussed on the basis of the structures and the electronic properties of these materials. This has allowed to propose the mechanism of the reaction when the hybrid is used. Moreover, the hybrid has an excellent performance which largely outperforms the results of the former hybrid [19]. This last result has also been discussed on the basis of the differences between the texture and electronic properties of both photocatalysts.

2. Experimental

2.1. Materials

A commercial graphene sample, G, (# 2191YJ) provided by Nano-Amor (USA) was used as precursor to prepare GSw. G is a few-layered graphene (sheet lateral sizes between 2 and 10 μm and 1–3 layers), with c.a. 3 wt% oxygen content, and has been already characterized by the authors [20,21,27]. All the solvents and the other chemicals used in this work were of analytical grade and used without any further purification.

2.2. Preparation of GSw

GSw graphene derivative has been obtained following a method previously described [21]. The preparation method is based on a two-step procedure consisting of a short exposition (5 min) of G to CS_2 microwave cold plasma. This results in a sulfur functionalized GS material, which was further treated with distilled water during 24 h to remove the labile sulfur functionalities, obtaining the final material GSw.

2.3. Preparation of GSw-Pd

GSw-Pd was obtained by suspending 0.0100 g of GSw in 20 mL of an 1 M KCl and $7.5{\cdot}10^{-4}$ M K_2PdCl_4 aqueous solution. The pH was fixed to 5.0 by HCl 0.1 M. The mixture was shaken in a thermostatic air-incubator at 298.1 K during 48 h. Then the solid was separated by filtration, washed with double distilled water and ethanol and air dried. The amount of Pd(II) in the resulting material GSw-Pd (0.83 at%, 6.48 wt%) was determined from the survey XPS spectrum.

2.4. Preparation of GSw-Pd-CdS

The GSw-Pd-CdS hybrid material was obtained by the slowly deposition of CdS on GSw-Pd up to the final amount of precipitated CdS was c.a. 95 wt% of the resulting material. This was carried out by adding 0.25 mL of 0.0235 M Na_2S and $Cd(CH_3COO)_2$ aqueous solutions alternatively to a stirred aqueous suspension of GSw-Pd (5 mg in 20 mL of water). Consecutive additions were needed to reach the desired amount of CdS (95 wt%) which were set up at 5 min time intervals between the additions. Then, the mixture was centrifuged and the resulting solid GSw-Pd-CdS was recovered by filtration, washed with water and ethanol, and dried at 110 °C for 8 h. This solid contains c.a. 4.5 wt% of GSw and c.a. 0.5 wt% of Pd.

2.5. Preparation of Pd-CdS

Pd-CdS was prepared in two steps. In the first one Pd^0 NPs were obtained by adding, drop by drop, 10 mL of a 2.5 M $NaBH_4$ aqueous solution to 50 mL of a 0.1 M Na_2PdCl_4 aqueous solution (molar ratio

$BH_4^-/PdCl_4^{2-} = 5/1$). The mixture was allowed to react under stirring for 30 min. The resulting black solid was separated by filtration, washed repeatedly with doubly distilled water, and dried in a desiccator under silica until a constant weight was obtained. In a second step, the Pd-CdS material was obtained by slowly CdS precipitation on Pd^0 NPs. The procedure was the same above described for the preparation of GSw-Pd-CdS. The resulting Pd-CdS material contains c.a. 0.7 wt% of Pd.

2.6. Preparation of CdS

CdS was prepared by mixing, in 1:1 molar ratio, saturated aqueous solutions of $Cd(CH_3COO)_2$ and Na_2S. The resulting solid was recovered by filtration, washed with water and ethanol and air dried.

2.7. Characterization

Several GSw data has been already reported. Moreover, the surface charge density (Q in mmol $H^+ \cdot g^{-1}$ of adsorbent) of GSw was determined from the potentiometric titration of the solid [28,29]. This was carried out in an aqueous suspension at 298.1 K, using $(CH_3)_4NCl$ 0.1 M and $(CH_3)_4NOH$ 0.1 M as background electrolyte and titrating agent, respectively [30]. The proton isotherm was obtained by plotting Q vs equilibrium pHs. The pKa distribution plot of the acid surface groups was obtained by analyzing of the proton isotherm with SAIEUS software [28].

X-ray diffraction (XRD) of the samples was performed at room temperature on a Panalytical Empyrean diffractometer using Cu-Kα radiation ($\lambda = 1.5406$ Å) over a 2θ angular range of 10–70°, at a scan rate of 5° min^{-1}.

The optical properties of the solids were studied through the UV–visible absorption spectra. The spectra were obtained in water dispersions when it was possible, i.e. for water dispersible samples. They were obtained in the 200–900 nm range, by using 1 cm quartz cells on a Perkin Elmer, Lambda 25, spectrophotometer. In the case of the low dispersible GSw-CdS and GSw-Pd-CdS the UV-visible diffuse reflectance spectra (DRS) were obtained on a Shimadzu UV-2600 spectrophotometer, over the 250–900 nm range, using $BaSO_4$ as a reference. Band gap energies of both direct and indirect electron transitions were calculated by analyzing the Tauc plots resulting from the Kubelka–Munk transformation of the UV-visible spectra [31].

The X-ray Photoelectron Spectroscopy (XPS) spectra were obtained in a Kratos Axis Ultra DLD spectrometer. Monochromatic Al/MgKα radiation in constant analyzer energy mode with pass energy of 160 and 20 eV (for the survey and high-resolution spectra, respectively) was used. The C 1s transition at 284.6 eV was used as a reference to obtain the heteroatoms binding energies. The accuracy of the binding energy (BE) values was ±0.2 eV.

Transmission electron microscopy (TEM) images, high-resolution transmission electron microscopy (HRTEM) images, selected area electron diffraction (SAED) patterns, energy-dispersive X-ray (EDX) spectra and mapping were collected by using a HAADF FEI TITAN G2 microscope. The resolutions were 0.8 Å and 1.4 Å in TEM and STEM mode, respectively. The microscope was operated with a working tension of 300 kV.

2.8. Photocatalytic experiments

The photocatalytic hydrogen production experiments were performed at 298.1 K and atmospheric pressure in a 140 mL doubled-walled flask, sealed with a silicone rubber septum. A solar simulator (PICO G2V Optics Inc.), providing a standard AM1.5 G light spectrum, was used as a visible light source to trigger the photocatalytic reaction under solar simulated conditions. In a typical experiment, 5 mg of the catalyst was dispersed in an aqueous solution (5 mL) of 0.35 M Na_2S and 0.25 M Na_2SO_3 as sacrificial agent. A continuous magnetic stirrer was applied at the bottom of the reactor in order to keep the photocatalyst in suspension. Prior to irradiation, the system was bubbled with argon for 20 min to remove the dissolved oxygen. In each experiment the suspension was irradiated for 8 h; during this time, 0.02 mL of the generated gas was collected through the septum for analysis at predesigned time intervals. The hydrogen content in the generated gas was analysed by gas chromatography (GC-Agilent Technologies 7820A, TCD, Ar carrier 5 Å molecular sieve column). Recycling tests of photocatalytic H_2 evolution were performed as follows to evaluate the stability of the photocatalyst. Typically, after a first run of 4 h under visible light irradiation by the solar simulator, the photocatalytic system was thoroughly degassed again, without the separation of the photocatalyst. Subsequently, the degassed system was irradiated again. The following runs of photocatalytic recycling tests were performed in the same way. The apparent quantum efficiency (AQE) of the H_2 evolution was measured with a 420 nm high power LED as light source. For this experiment, the photoreactor (containing 30 mg of phtocatalyst in 5 mL of 0.35 M Na_2S and 0.25 M Na_2SO_3 aqueous solution, at 298.1 K and atmospheric pressure) was placed 1 cm away from the LED source. The moles of incident photons in unit time ($1.8 \cdot 10^{-7}$ einstein$\cdot s^{-1}$) were measured by chemical actinometry, using potassium ferrioxalate as actinometer [32,33]. The AQE (%) was calculated according to the following equation:

$$\text{AQE}\ (\%) = \frac{\text{number of reacted electrons in unit time}}{\text{number of incident photons in unit time}} \times 100$$

$$= \frac{\text{2x number of evolved } H_2 \text{ molecules in unit time}}{\text{number of incident photons in unit time}} \times 100$$

3. Results and discussion

3.1. Characterization of GSw

The Raman spectrum of the precursor, G, already reported [21] shows a relatively large intensity of the D band. This fact, together with the size of the sheets is relatively small (between 2 and 10 μm), points out that G contains significant amount of irregularities and defects that should be mainly placed at the edge of the sheets [19,21,27]. The treatment of G with CS_2 cold plasma during 5 min, followed by water washing of the obtained solid during 24 h (Section 2.2) results in a solid, GSw containing c.a. 1.5 at% of S (mainly as C-S-C and C-S-H, and small amounts of C-SO-C and C-SO_2-C) and c.a. 6 at% of O [21]. According to both Raman and XPS data the treatment does not result in significant increase of defects in the precursor G neither alters the extension of the sp^2 moieties [21] that remains unaffected after the treatment. This suggests that most of the sulfur containing functionalities in GSw are also probably placed at the edge of the defects [21].

To get further insight into the (Brønsted) acid-base properties of the GSw surface the proton isotherm was obtained in water solution (see Section 2.7). The analysis of the isotherm data with the SAIEUS software allows to obtain the pKa distribution values (Fig. 1). Most of the positive surface charge at the onset of the titration is assigned to protonation of Cπ centres of the graphene surface, i.e. to $C\pi \rightarrow H_3O^+$ interactions [34]. This assignment is based on the sulfur and oxygen containing groups remaining after the plasma treatment, lack Brønsted basic character.

This charge is significantly smaller in GSw (c.a. 2.5 mmol H^+ per gram) than in the precursor G (c.a. 5.0 mmol per gram) [27]. This is probably due to the removal of carboxylate and hydroxyl oxygen functions by the CS_2 plasma treatment which reduces the protonation sites of GSw. This statement is based on the functionalization with S neither increases the number of defects nor decreases the extension of conjugated sp^2 system [21]. This is an important point as it has been pointed out that sp^2 moiety is crucial in water reduction with photocatalysts supported on graphene. This results in the point of zero charge (pzc) of GSw (7.7, see Fig. 1a) is slightly smaller than that of G (8.6) [27]. In contrast to the surface of the precursor G, Fig. 1b shows that the surface of GSw lacks carboxyl groups (with pKa < c.a. 3.0). This suggests that

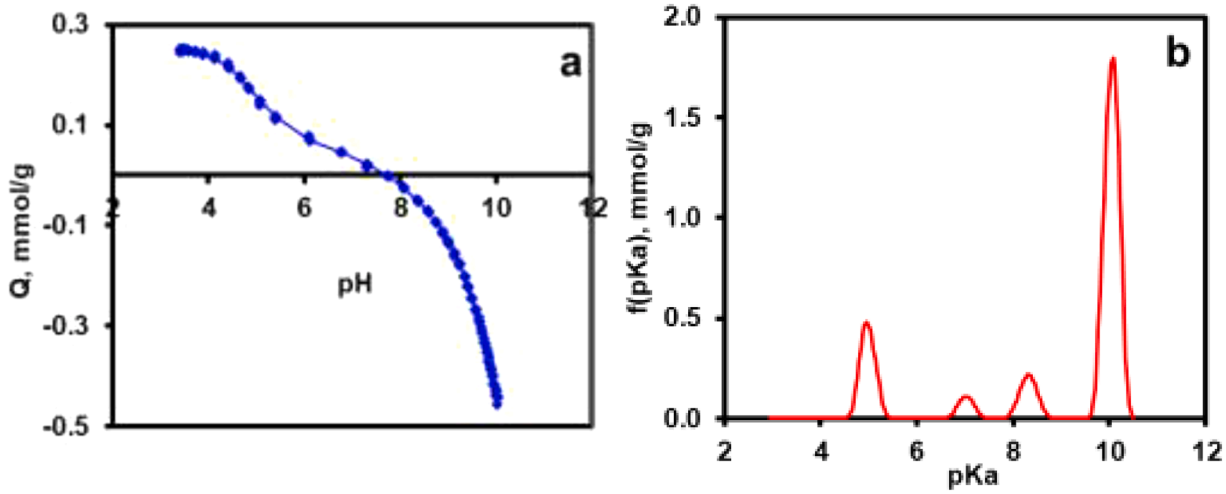

Fig. 1. a) Plot of surface charge density values of GSw (Q in mmol of H^+per gram) as a pH function; b) plot of pKa values of the surface acidic groups of GSw.

the CS_2 plasma species mainly react with the oxygen containing groups of the precursor G. The pKa peaks at c.a. 4.9, 7.0, 8.3 and 10.0 are assigned to deprotonation of the groups resulting from disaggregation of unstable thiocarboxylate/anhydride groups, neutralization of H_3O^+ attached to Cπ moieties and thiophenol and thiocarboxylate, respectively.

The UV-visible spectrum of GSw in aqueous suspension (Fig. 2a) was obtained to have additional information about its electronic properties. In the UV range, GSw shows an intense band at c.a. 280 nm, (like G), but also a shoulder at c.a. 220 nm which is absent in G spectrum [19]. According to the literature the band at c.a. 280 nm, characteristic of few-layered graphene, is due to plasmon π-π* transitions from the sp^2 domains. Both the asymmetry of the band at 280 nm and the shoulder at c.a. 220 nm probably merge from n−π* transitions (which usually appear at c.a. 310−320 nm) of non-bonding electrons of the conjugated oxygen and sulfur atoms, respectively [35,36]. The broad absorbance in the whole visible range is typical of graphene [37].

The plots (Fig. S1) of the square and square root of αE (where α = absorbance and $E = h\upsilon$) vs hυ [31] obtained from the GSw UV-visible spectrum do not show any absorption edge (which is similar to this of G) [19,27]. This suggests the absence of any energy gap between the valence and conduction bands, i.e. most of the extended sp^2 system remains after the treatment of G with CS_2 plasma. This means that the overlapped π bonding and π^* antibonding orbitals are not split which is also consistent with the lack of hole defects in GSw sheets [21].

In spite of its limited lateral resolution XPS is a reliable technique to measure the work function of graphene, ϕ, in the energy scale of this technique [38]. The relative values of the work function of the components of the hybrid photocatalysts are useful to stablish suitable electronic diagram which can help to get insight into the possible mechanism of the catalytic process. From the XPS spectrum of GSw in the VB region, a value of −0.29 eV for its work function is obtained (Fig. 2b).

3.2. Characterization of GSw-Pd

As already commented in the experimental section, the preparation of the GSw-Pd-CdS hybrid photocatalyst was carried out through two steps. Firstly, the GSw-Pd material was obtained and then it was used as support to obtain the final GSw-Pd-CdS material by slow precipitation of CdS. This section is focused on the characteristics of GSw-Pd.

The Pd content in GSw-Pd obtained from the survey XPS is 0.83 at% (Fig. S2). The TEM images of GSw-Pd in Fig. 3 (a and b) show a homogeneous distribution of very small particles deposited on GSw sheets which, according to the EDX spectrum of Fig. 3c and XPS analysis, correspond to Pd aggregates. The size of the particles was analysed statistically with ImageJ software [39] from which a mean particle size between 1 and 2 nm was obtained (inset in Fig. 3b).

In addition, it is seen in Fig. 3b that more than 95 % of the particles has sizes smaller than 3 nm, i.e. almost the whole of the palladium deposited on the surface of GSw are small-size palladium clusters. Moreover, Fig. 3d clearly shows the homogeneous distribution of the

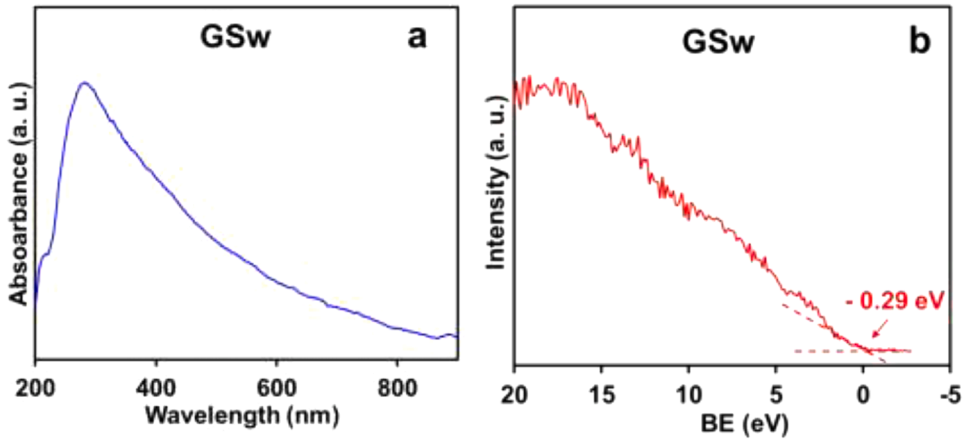

Fig. 2. a) Uv-visible spectrum of GSw; b) XPS valence band spectrum and value of the work function of GSw.

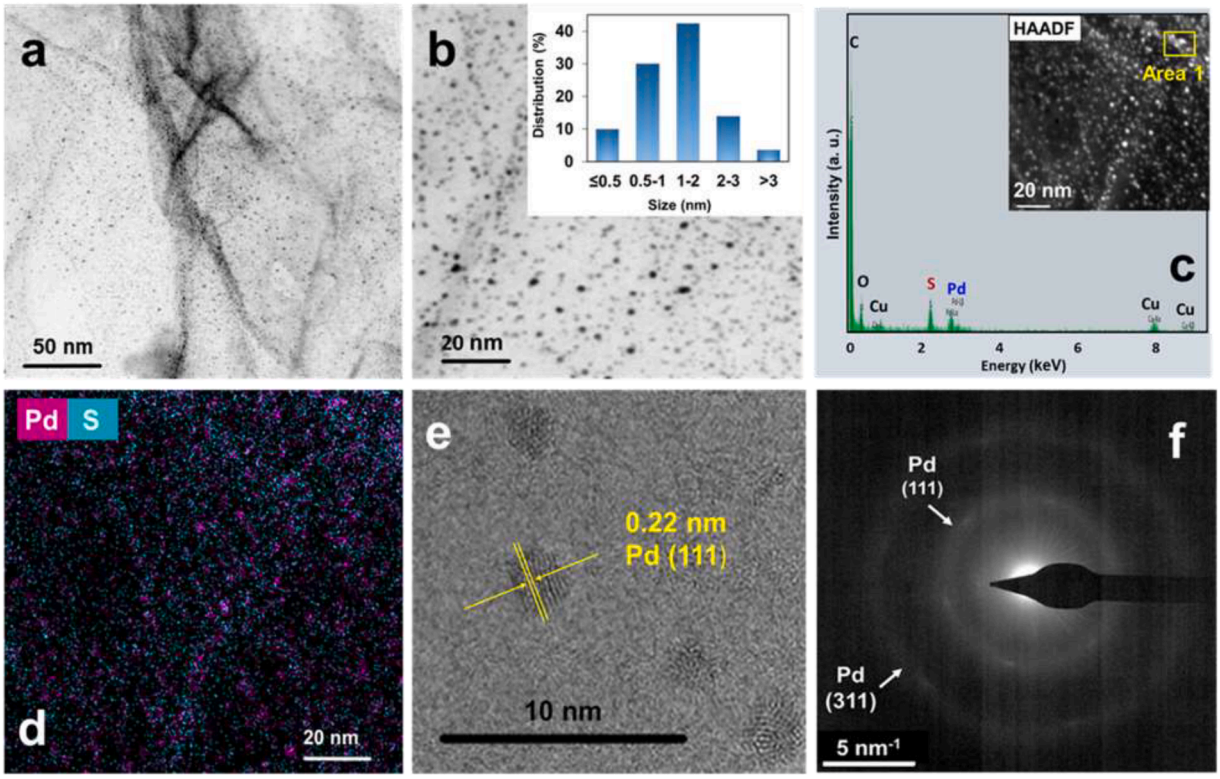

Fig. 3. Images and spectra of GSw-Pd obtained by HRTEM: a) and b) TEM images and Pd particle distribution sizes (inset Fig. 3b); c) EDX spectrum; d) element distribution map; e) HRTEM image and f) SAED pattern.

pair sulfur/palladium on the graphene surface. This suggests that the deposition of most Pd on the GSw surface is mainly driven by the bonding to sulfur functions which results in the formation of clusters [21,23]. Having in mind the outstanding advantages for photocatalytic applications of metal nanoparticles having both small sizes and good crystal quality, it can be expected the GSw-Pd structure is suitable for photocatalytic application [40].

Magnified HRTEM images of GSw-Pd (Fig. 3e) show crystals of Pd clusters in the 2–3 nm range which were obtained for further analysis of its morphology. In most of the crystals some irregularities due to apparent mixed crystal phases or defects in their morphology, prevent from accurate measurement of interplanar spacing. This can be observed in Fig. 3e together to a lonely crystal displaying lattice fringes with interplanar spacing of 0.22 nm, which can be assigned to (111) crystallographic planes of the Fm3m cubic symmetry group, typical of clusters with the above sizes [40]. The selected area electron diffraction (SAED) pattern (Fig. 3f) also shows two diffraction rings (with 16.8 nm^{-1} and 9.5 nm^{-1} diameters) corresponding to (111) and (311) Pd planes [AMCDS code 0011155]. It must be hightligted the very small sizes of the Pd clusters and their homogeneous distribution on the GSw surface favour both the efficient absorption of radiation and the stability of the Pd phase. These facts will lead to an efficient catalytic cooperation with the other two components of the GSw-Pd-CdS catalyst.

The data obtained from the XPS spectra of both GSw and GSw-Pd provide additional information about their composition and the chemical nature of the components. The survey spectrum of GSw-Pd, (Fig. S2) shows C, O, S, Pd, and Cl as significant components of this material. The amount of Pd is much higher than the one the parent G is able to adsorb under similar conditions [21]. This points out to the role of the sulfur containing groups of GSw have for the capture of Pd. The Cπ centres on the graphene surface are also active sites for the planar adsorption of $PdCl_4^{2-}$, via Cπ-π interactions [41]. Nevertheless, the small amount of Cl in GSw-Pd (Fig. S2) indicates that only a residual amount of Pd has been adsorbed through the Cπ-π mechanism.

The S 2p high resolution XPS spectrum of GSw-Pd (Fig. 4a) consists of two main components, due to spin-orbit coupling ($2p_{1/2}$ and $2p_{3/2}$, respectively). This spectrum can be deconvoluted into four doublets, corresponding to four S functions [21]. The doublet with peaks at 162.4 eV (due to S $2p_{1/2}$) and 163.6 eV (due to S $2p_{3/2}$) is assigned to C-SH groups. These binding energies are shifted to smaller values compared to the same function in GSw (163.8 eV and 165.2 eV) [21] which is due to the C-SH/Pd interactions. A similar effect has been already reported for the same C-SH functions in GO when Pd is added forming 2–3 nm clusters [23]. The doublet at 164.0 eV and 165.2 eV (which is assigned to C-S-C groups) is almost unshifted compared to the same groups in GSw (163.7 eV and 164.9 eV), which points out that these groups barely retain Pd atoms. The doublets assigned to C-SOC and C-SO_2-C functions in GSw-Pd at 167.9 eV-169.1 eV and 169.0 eV-170.1 eV respectively, are also shifted to larger BE values compared to GSw (165.0 eV-166.2 eV and 168.0 eV-169.2 eV) [21]. This means that these functions also take part in the stabilization of Pd clusters. This is consistent with literature data about the ability of ligands bearing both R-SO and R-SO_2 functions to bind Pd(II) by S acting as donor atom [42–44].

The oxygen contents of GSw, 5.18 at% and GSw-Pd, 8.23 at%, were obtained from the survey XPS spectra (Fig. S2). The O 1s high resolution XPS spectrum of GSw (Fig. 4b) contains two main components; one at 534.3 eV, assigned to R-SO and R-SO_2 functions, and the other one at 532.4 eV, due to R1-CO-R2 functions. A weak component at 536.2 eV, is assigned to H_2O adsorbed on graphene surface [45]. Deconvolution of the high resolution O 1s spectrum of GSw-Pd (Fig. 4d) shows a component at 532.1 eV ascribed to R1-CO-R2 functions. Its relative intensity is higher than in GSw spectrum (Fig. 4b) suggesting that the added oxygen is included in this component whose BE value points out that doesnt correspond to water attached to the graphene surface. Moreover the BE value of 532.1 eV fits that of the oxygen attached to Pd [45]. Finally, a slightly increased intensity of the water component (at 535.9 eV) of GSw-Pd relative to the GSw also accounts for the above mentioned increase in oxygen content. The third component in the O 1s

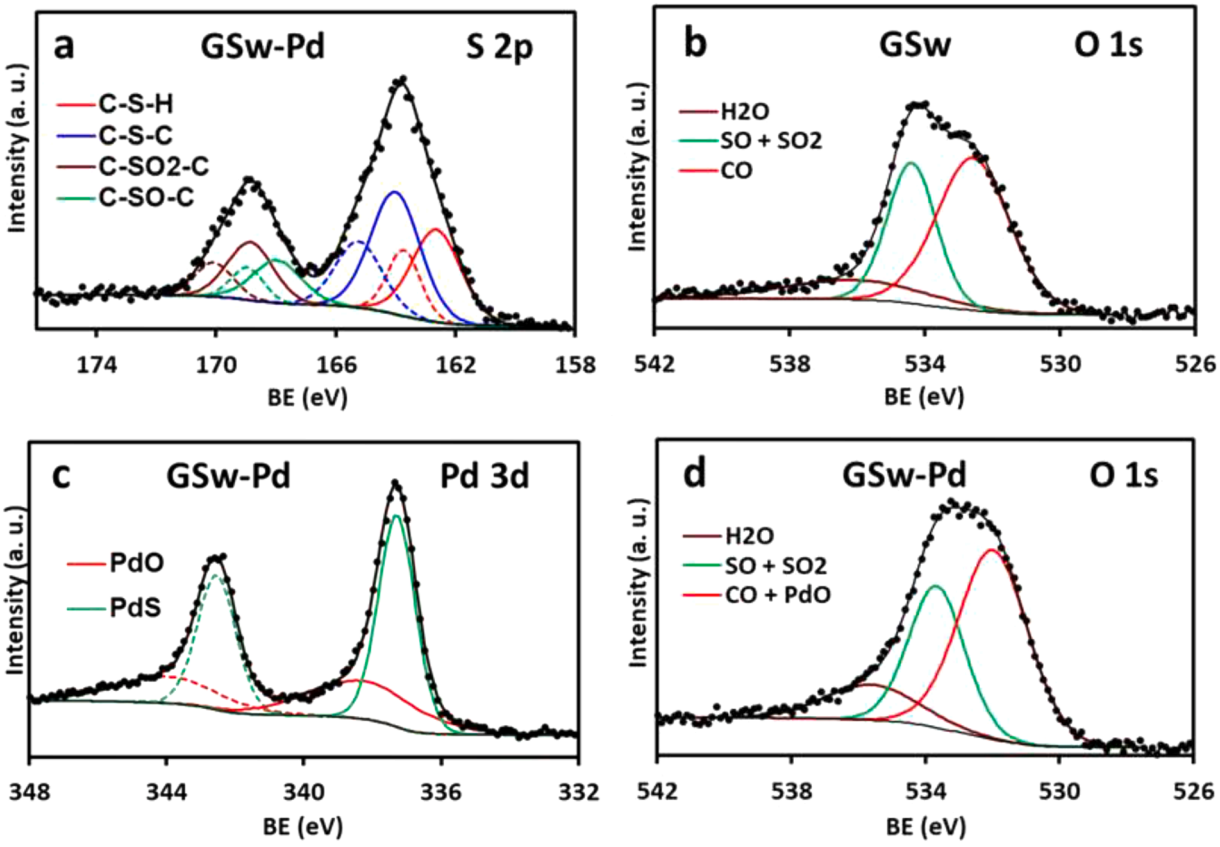

Fig. 4. High resolution XPS spectra of: GSw-Pd in the S 2p, Pd 3d and O 1s regions (a, c and d, respectively), GSw in the O 1s region (b).

high resolution spectrum of GSw-Pd, at c.a. 534.0 eV, is assigned to R-SO and R-SO_2 functions.

The Pd 3d high resolution spectrum of GSw-Pd (Fig. 4c) consists of a doublet due to Pd $3d_{5/2}$ and Pd $3d_{3/2}$ states. Deconvolution of the doublet results in two components; a pair with peaks at 337.3 and 342.6 eV and a second one with peaks at 338.3 and 344.0 eV. These values are in a higher range than those given in the literature for Pd(0) whilst fit better those given in the literature for Pd-O in total/partially oxidized Pd clusters, namely at c.a. 335 eV and 340 eV [23,40,46,47]. Thus the above data point out that the nature of Pd in the GSw-Pd material consists of Pd-PdO core-shell clusters. According to this it should be expected three chemically different Pd atoms: i) those linked to oxygen at the more external shells of the clusters, ii) those linked to S-functions, and iii) those at the inner core of the clusters. Nevertheless, the deconvolution of the signals (Fig. 4c) results in two components. Thus, the insignificance of a component due to Pd(0) at the core the clusters that should appear at values of BE smaller than the two others could be due to they are difficult to be reached by radiation. The peak at c.a. 4 eV seen in the XPS VB spectrum of GSw-Pd (Fig. 5a), which is not seen in the XPS VB spectrum of the precursor GSw (Fig. 2b), is assigned to the electrons evolved from the Pd nanoclusters. The energy of the work function of this phase, 0.97 eV, obtained from the tangent at the onset of the signal, is slightly higher than the one of the GSw, −0.29 eV. In summary, the whole XPS data are consistent with the nature of Pd in the GSw-Pd material consists of Pd clusters and Pd-PdO core-shell clusters.

It was attempted to get more insight on the nature of Pd species in clusters through XRD, but probably due to the low Pd content in GSw-Pd sample it was not detected in its XRD any other peak than those of GSw support [22] (Fig. S3).

The UV-visible spectrum of GSw-Pd was obtained in aqueous

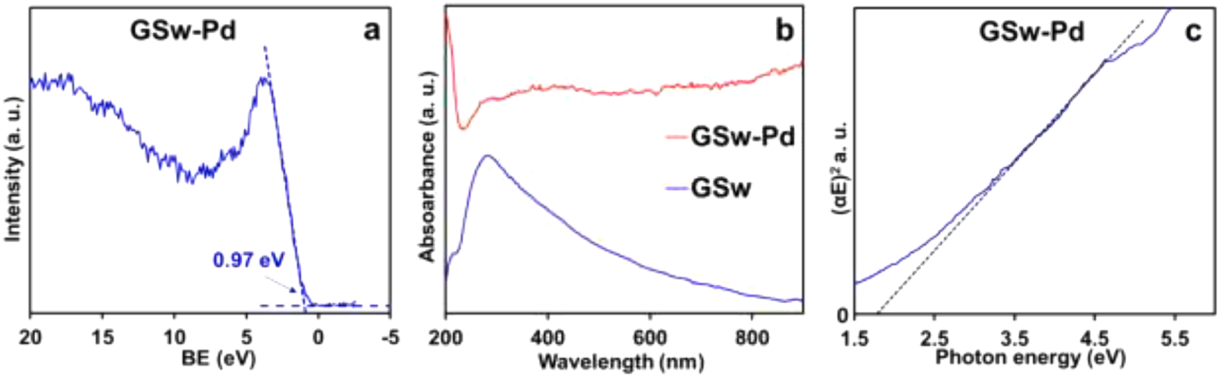

Fig. 5. a) XPS valence band spectrum and value of the work function of GSw-Pd; b) UV-visible spectrum of GSw-Pd (together with the spectrum of GSw); c) plot of $(\alpha E)^2$ vs photon energy (direct transitions) for GSw-Pd.

suspension to get insight into the optical properties of this material under similar conditions to those used in the photocatalytic water reduction. GSw-Pd shows higher background absorption than GSw in the whole 200–750 nm range which gives rise the absorption bands arising from GSw in the UV range to be hidden (Fig. 5b). This fact is in accordance with the very little size of Pd clusters existing in GSw (most of them having sizes varying in the 0.5–3.0 nm range). Thus, the wide absorption should be adscribed to electron transitions between states of the Pd clusters, whose non uniform sizes lead to a wide wavelength absorption range. It has been also pointed out that in the case of Pd nanoclusters with sizes $>$ 4 nm it should be expected absorption due LSPR at values of c.a. 700 nm [47], however this shouldnt be probable in the case of GSw-Pd due to clusters having these sizes are insignificant (see Fig. 3b). From the UV–vis spectrum of GSw-Pd, a direct transition at c.a. 689 nm (1.8 eV) is detected in the Tauc plot of Fig. 5c.

In summary, the above data show that the adsorption of Pd on GSw results in a really uniform covering of its surface with very small and homogeneous Pd nanoclusters (c.a. 97 % with sizes smaller than 3 nm). This type of metal/layer-structures is crucial in the electrocatalytic activity of water oxidation of other noble metal nanoparticles deposited on thiolate supports [48,49]. The GSw-Pd hybrid shows significant increase of absorption in the UV-visible range compared to GSw. It is expected this increase favours its efficiency as cocatalyst in water reduction when it is combined with CdS. For this task it is necessary the energy of Pd nanoclusters HOMO and LUMO systems suitably aligns with that of the CdS VB and CB, so allowing charge transfer between the two phases [50, 51].

3.3. Characterization of GSw-Pd-CdS

The GSw-Pd-CdS hybrid (95 wt% CdS) was obtained by slow precipitation of CdS on the solid GSw-Pd (see Section 2.4). The TEM images and the element distribution map of GSw-Pd-CdS (Fig. 6) show small Pd nanoclusters of quite uniform sizes also very uniformly distributed on the GSw surface. CdS appears forming crystal aggregates of different sizes deposited on the Pd clusters which results in close contact between both phases. The average size of the CdS aggregates on the surface of GSw-Pd is significantly smaller than this obtained by a similar procedure in absence of a graphene support (see Fig. S4). This points out that the graphene/CdS nanoparticles interaction probably limits their aggregation. The crystal nature of CdS phase is observed in the magnified HRTEM images of Fig. 6c and d obtained from selected areas of crystal aggregates. The images display lattice fringes with interplanar spacing of 0.33 nm and 0.17 nm, which can be assigned to (111) and (311) crystallographic planes of cubic CdS (COD code 1011260; AMCSD code 0018121). Moreover, interspacing plane values of 0.24 nm and 0.35 nm, assigned to (102) and (100) planes of hexagonal CdS (COD code 1011054; AMCSD code 0017955) are displayed in Fig. 6c. Thus, both CdS crystal forms are present in the GSw-Pd-CdS hybrid.

The selected area electron diffraction (SAED) pattern of Fig. 6d indicates the presence of nanocrystals of CdS. Three of the inside diffraction rings in Fig. 6d (those with 5.98, 9.86 and 11.61 nm^{-1} diameters) are due to (111), (220) and (311) planes of the cubic CdS. None of the diffraction rings in Fig. 6d belong to hexagonal CdS, which means that most of the CdS crystals are cubic whereas the hexagonal phase is a minor component. This is clearly seen in the XRD pattern in Fig. 7. This Fig. shows diffraction peaks at 26.7°, 44.2° and 52.0° assigned to the (111), (220) and (311) planes of the cubic CdS [7] (COD code 1011260; AMCSD code 0018121) and much weaker peaks of hexagonal CdS component at 23.5°, 26.9°, 30.2°, 36.4°, 43.7°, 48.0°, 49.8°, 52.2°, 58.2° and 65.5°corresponding to (100), (002), (101), (102), (110), (103), (200), (112), (202) and (203) planes (COD code 1011054; AMCSD code 0017955) [52]. The diffraction peaks of graphene and Pd are not evident which is probably due to they are in very small amounts in the hybrid (see Section 2.4). Moreover, the fact that Pd is not seen neither in the HRTEM images nor in the SAED pattern (Fig. 6) nor in XRD (Fig. 7) is

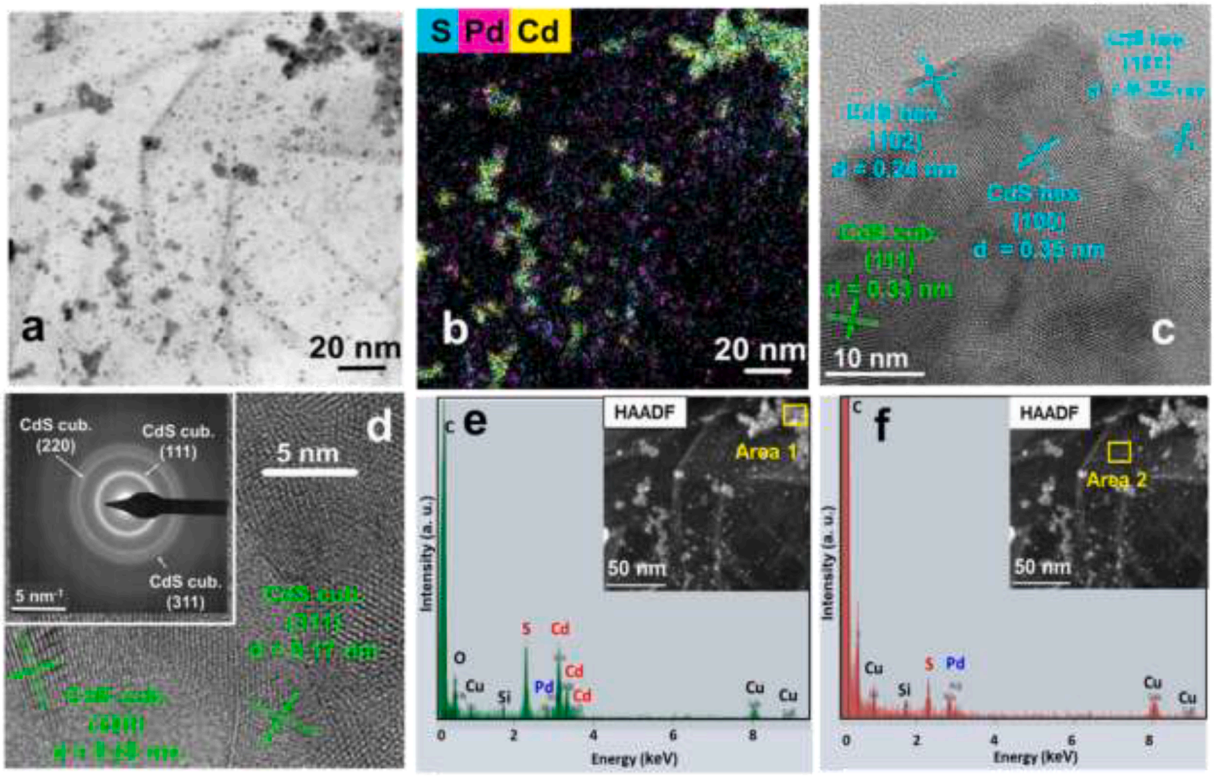

Fig. 6. Images and spectra of GSw-Pd-CdS obtained by HRTEM: a) TEM image; b) element distribution map; c) and d) HRTEM images and SAED pattern (inset Fig. 6d); e) and f) EDX spectra.

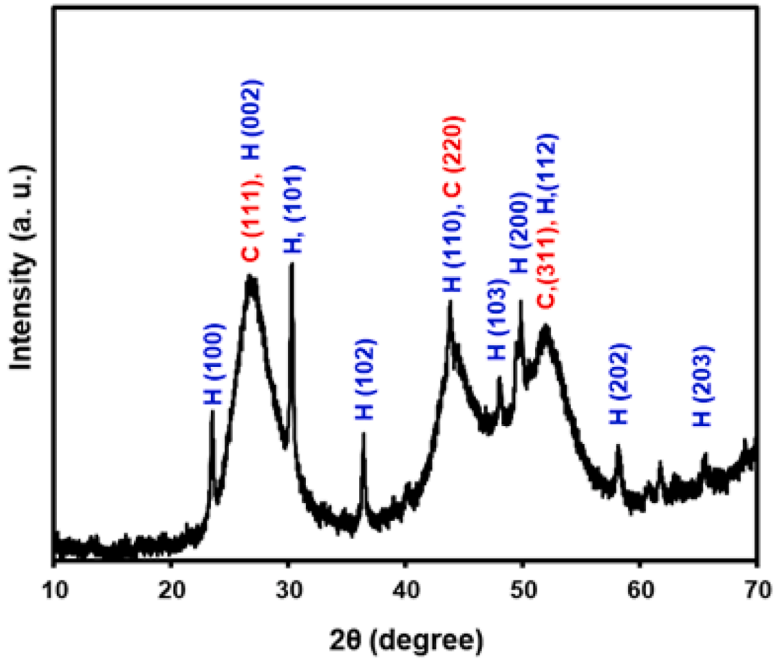

Fig. 7. XRD pattern of GSw-Pd-CdS showing XRD peaks assigned to hexagonal CdS (H) and cubic CdS (C).

probably due to these data were obtained from an area where the CdS crystals cover the Pd clusters avoiding the radiation to reach them. This is seen in the EDX analysis of two selected areas of Fig. 6e and f. Thus, in area 1 (Fig. 6e) it is seen the main component is CdS whereas in area 2 (Fig. 6f) no CdS is evident and only Pd is seen.

Nevertheless, although Pd is a minor component of GSw-Pd-CdS, its HR XPS spectrum in the 3d region (Fig. 8a) shows a well-defined double signal, with maxima at 337.2 eV and 342.5 eV, very similar to that of the GSw-Pd precursor (Fig. 4c). This suggests that the deposition of CdS on the GSw-Pd surface doesn't affect the nature of the Pd clusters which remain attached to surface by the sulfur containing functions. Moreover, the HR XPS spectrum of GSw-Pd-CdS in the S 2p region (Fig. 8b) consists of a wide intense double signal with two components at c.a. 162.0 eV and 163.0 eV, assigned to 2 $p_{1/2}$ and 2 $p_{3/2}$ of CdS [45]. Furthermore, it is present another weak wide signal at c.a. 169.0 eV, which is assigned to the satellites of these two components and which is indicative of the semiconductor character of the CdS crystals [53]. Due to CdS is the major component of Gsw-Pd-CdS, their S signals hide those of sulfur in GSw-Pd (with peaks at c.a. 164 eV and 169 eV, see Fig. 4a) as both have similar energies, although these lasts are evidenced on deconvolution of the signal (Fig. S5). In the Cd 3d range (Fig. 8c) there are two signals at 405.6 eV and 412.3 eV which correspond to the 3 $d_{5/2}$ and 3 $d_{3/2}$ component of Cd(II) species [45,54]. A signal in the C 1s region (with maximun at 284.6 eV, Fig. 8d) confirms that graphene is a component of the Gsw-Pd-CdS hybrid. Deconvolution of this signal show that besides C sp^2 and C sp^3 components those corresponding to carbon linked to sulfur

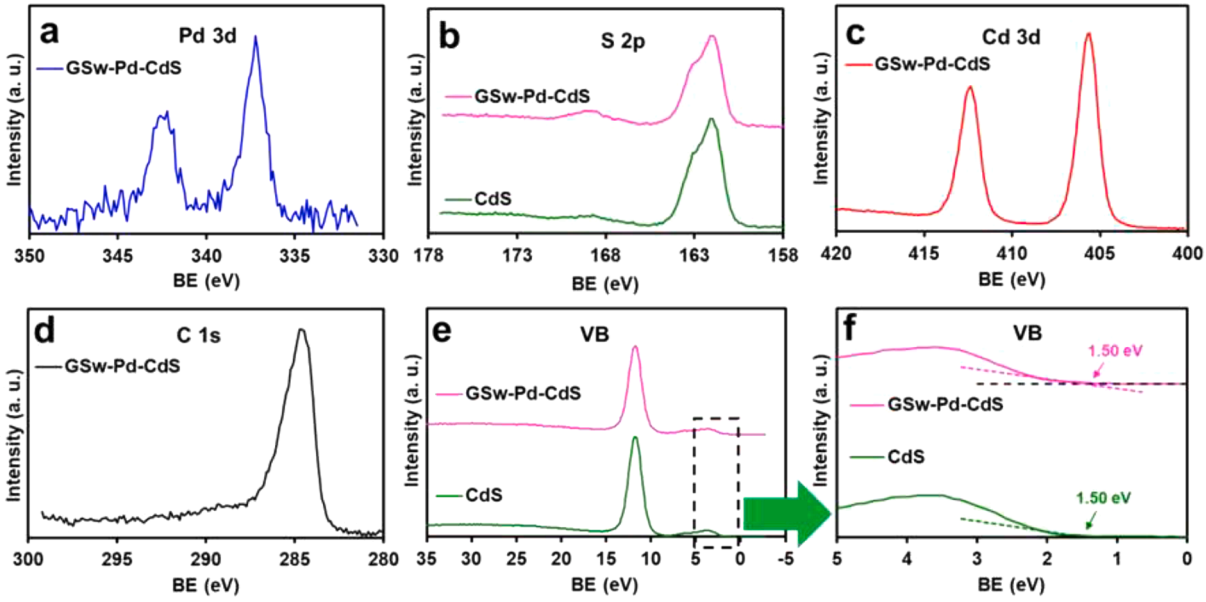

Fig. 8. High resolution XPS spectra of: i) GSw-Pd-CdS in the, Pd 3d, Cd 3d and C 1s regions (a, c and d, respectively) and ii) CdS and GSw-Pd-CdS in the S 2p and valence band regions (b, e, and f).

functions existing in the precursor GSw are also preserved in GSw-Pd-CdS, as shown in Fig. S6.

The XPS spectrum in the VB range of GSw-Pd-CdS only shows the band due to CdS (Fig. 8e). The onset energy of the weak signal at the smallest energy range corresponds to the highest electron energy in the VB of the semiconductor CdS [55]. This value, 1.50 eV, has been obtained from the intersection of the tangent to the onset of this signal with the BE axis, as depicted in Fig. 8f, and is similar to that obtained from the spectrum of the bare CdS.

The UV-visible diffuse reflectance spectrum of GSw-Pd-CdS and this of CdS are shown in the Fig. 9a. The CdS spectrum shows high absorption values in the 250–500 nm range which sharply decreases reaching almost insignificant absorbance values in the 600–800 nm range. The spectrum of GSw-Pd-CdS also shows that the absorbance in the 250–500 nm range is a bit higher than this of CdS. This is probably due to the main contribution comes from CdS (the major component of this material, 95 wt%) but also from both Pd clusters and GSw. Nevertheless, in contrast to CdS, the absorption of GSw-Pd-CdS in the 600–800 nm region is very significant. This is assigned to the absorption of both Pd clusters and GSw moieties, despite the amounts of both in the hybrid are small (c.a. 0.5 wt% and 4.5 wt%, respectively). The Tauc plots [31] of CdS and GSw-Pd-CdS are shown in Fig. 9b and c, respectively. The comparison of both Fig. shows that the direct transition at 494 nm (2.56 eV) in the case of GSw-Pd-CdS (Fig. 9c) is due to the band gap transition of the CdS component (Fig. 9b). The fact that the amount of CdS in GSw-Pd-CdS (95 wt%) largely exceeds that of Pd nanoclusters (0.5 wt%), is probably the reason explaining the expected defined edges from electronic transitions of Pd are not seen.

3.4. Photocatalytic studies

As stated in the introduction section, in a previous study it was found that the photocatalytic activity in water reduction reaction of a hybrid consisting of CdS, a polyamine-functionalized graphene and PdS (labelled as G-Tren-PdS-CdS) shows notable results in this reaction [19]. In spite of its excellent catalytic performance it was found, as discussed in the Section 1, that the sheets of the polyamine functionalized graphene (G-Tren) tend to stack one to other and stacking is assumed to be a factor that limits the photocatalytic performance to some extent. The new hybrid GSw-Pd-CdS, containing a S-functionalized graphene derivative as support (GSw), which exhibits lower trend to stacking and high affinity to palladium [21], has been prepared and essayed as photocatalyst in the water reduction reaction.

The results of the photocatalytic activities in the water reduction reaction vs time, and the average amounts of H_2 produced when GSw-Pd-CdS, Pd-CdS, GSw-Pd and GSw are used as photocatalysts, are summarized in Fig. 10a and b, respectively. The photocatalytic activity of CdS is also included in Fig. 10b for comparative purpose. The very low dispersibility in water of non-functionalized graphene G (precursor of GSw) [19] probably caused unsuccessful attempts to obtain isolated G-CdS and G-Pd-CdS phases, so their photocatalytic activity could not be considered for comparative purposes. For the reduction of holes in the photocatalytic studies a mixture of Na_2SO_3 and Na_2S in water solution (instead only Na_2S) has been used, so preventing the formation of undesired S_2^{2-} occurring in the last case, as S_2^{2-} ions compete with the protons in the reaction with the photogenerated electrons [11].

The results show the excellent photocatalytic behavior of GSw-Pd-CdS in water reduction (3.79 mmol H_2 g^{-1} h^{-1} in average) which outperforms that of CdS by a factor of 31.1. Moreover, the AQE value (%) of GSw-Pd-CdS was calculated as 15.9 % at 420 nm. Fig. 10c shows that the production of H_2 slightly increases with time among the first two cycles up to a constant value which remains constant in the three last ones. The C, Pd, Cd and S high resolution XPS spectra of the fresh and used (for 20 h) GSw-Pd-CdS hybrid (Fig. S7) are very similar indicating that there are not chemical changes after being used. In addition, the C/S, C/Pd and C/Cd ratios obtained from the survey XPS spectra of both the fresh and used catalyst are very similar (Fig. S8). These two facts point out that the smaller H_2 evolution during the two first reaction cycles (Fig. 10c) is not the result of the photocatalyst degradation. It is likely the trend of the two first cycles is related to the ability of Pd to irreversibly absorb hydrogen, even at room temperature, which occurs during these cycles up to saturation [47].

The relative positions of energy levels of the GSw-Pd-CdS, GSw, Pd and CdS components are essential to explain their role in the photocatalytic reaction. For this purpose, the VB energy value (E_{VB}) of CdS was firstly calculated in the vacuum scale by using the Mulliken equation:

$$E_{VB} = X - E^e + 0.5E_g$$

where E^e is the energy of free electrons vs hydrogen (4.5 eV), X is the electronegativity of the CdS semiconductor, which is calculated from those of the ionization potential and the electronic affinities of their atomic components (S and Cd), and E_g is the band gap value obtained from the Tauc plot (2.56 eV, Fig. 10c) [19,56,57]. The calculated E_{VB} value relative to vacuum was −6.3 eV and that of CB, obtained from E_g, −3.8 eV. Although tentatively, (due to lateral resolution of XPS spectrum of c.a. 10 μm) [38], the XPS spectra of GSw and GSw-Pd in the VB region (Figs. 2b and 5a) allow positioning of both the work function (ϕ) of the former (−0.29 eV), and the energy of the HOMO of the Pd-clusters of the latter (0.97 eV) in relation to the VB energy of CdS as determined by its XPS spectrum in the VB range (1.50 eV, Fig. 8f) [55]. So, according to these data, the VB energy of CdS differs by 1.79 eV from the energy of the work function of GSw and by 0.53 eV from the energy of the HOMO of the Pd-clusters. Assuming that the energy of its different components is kept in the GSw-Pd-CdS hybrid, its electron diagram is that of Fig. 11a.

This diagram allows explaining the possible role played by each of the components of the GSw-Pd-CdS hybrid in the photocatalytic water

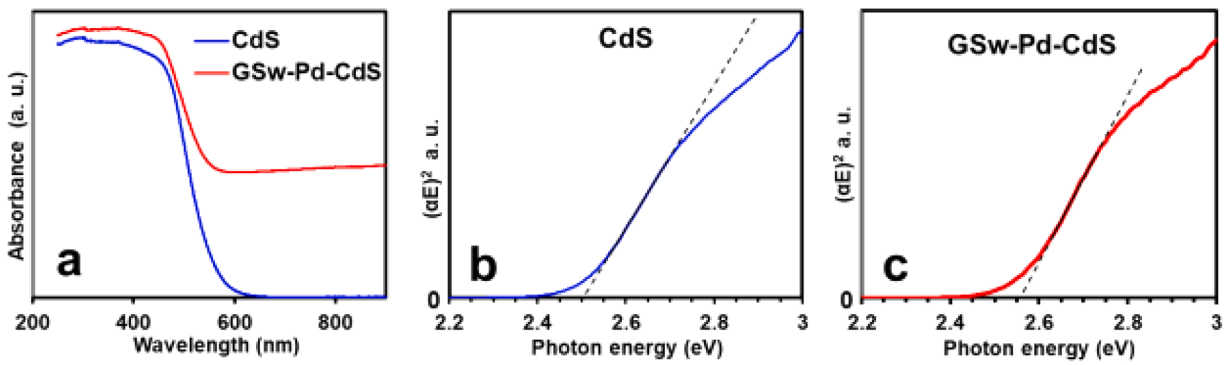

Fig. 9. a) UV–vis absorption spectra of CdS and GSw-Pd-CdS; b) plot of $(\alpha E)^2$ vs photon energy (direct transitions) for CdS; c) plot of $(\alpha E)^2$ vs photon energy (direct transitions) for GSw-Pd-CdS.

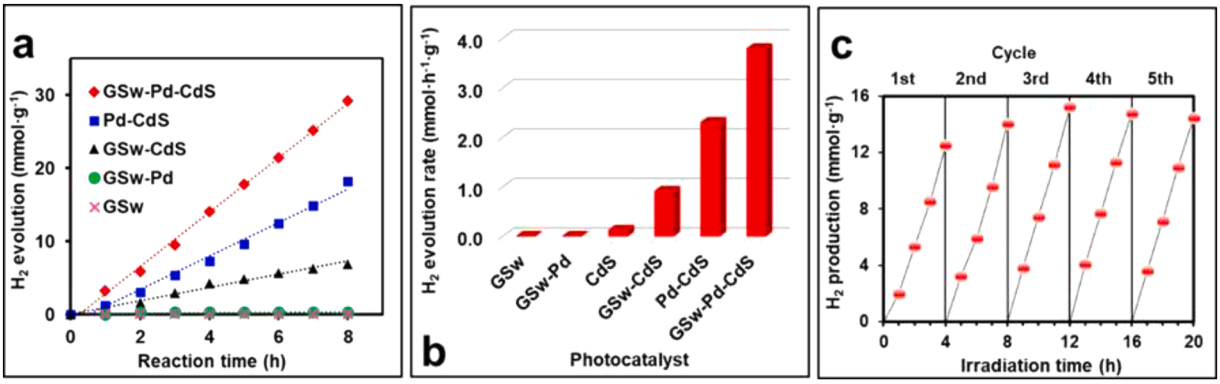

Fig. 10. Photocatalytic activity in water reduction reaction under visible light irradiation, using $5{\cdot}10^{-3}$ g of the corresponding photocatalyst in 0.35 M Na_2S/0.25 M Na_2SO_3 mixed aqueous solution: a) hydrogen evolution for GSw-Pd-CdS, Pd-CdS, GSw-Cd, GSw-Pd, and GSw catalysts; b) comparison of the photocatalytic H_2-production activity during 20 h of samples GSw-Pd-CdS, Pd-CdS, GSw-Cd, CdS, GSw-Pd, and GSw and c) cycling test of photocatalytic H_2 evolution for the GSw-Pd-CdS photocatalyst.

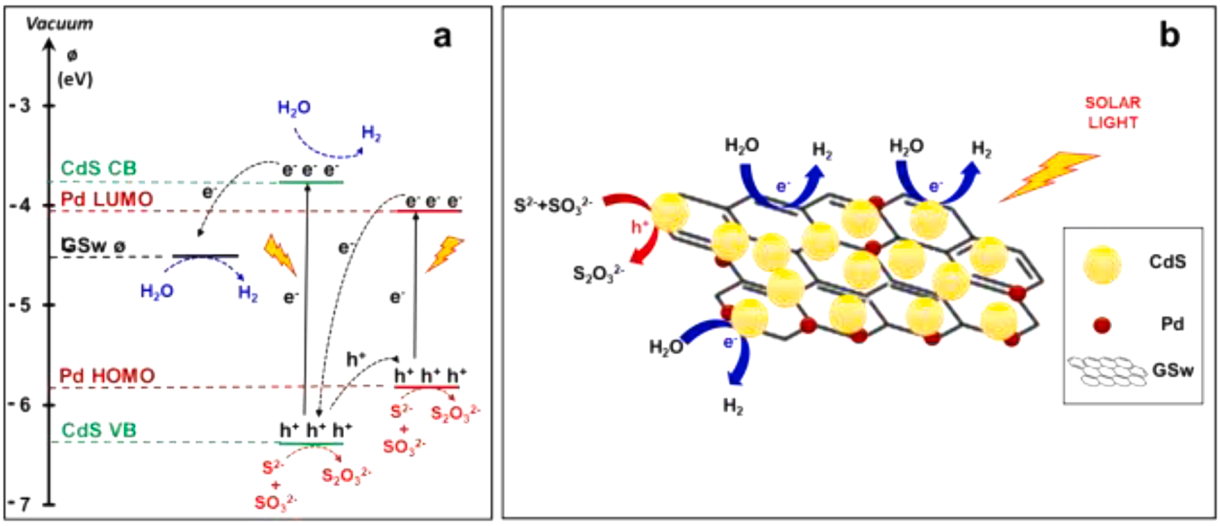

Fig. 11. a) Schematic energy diagram of GSw-Pd-CdS photocatalyst; b) schematic illustration for water reduction process with GSw-Pd-CdS photocatalyst.

reduction reaction (Fig. 11). For this purpose, the photocatalytic performance in water reduction of GSw, GSw-Pd, GSw-CdS and Pd-CdS is analysed. In these cases, the same experimental conditions as in the case of GSw-Pd-CdS hybrid were used.

According to the electronic diagram of Fig. 11a, the alignment of the GSw work function and the hydrogen reduction energies points out that the electrons excited in the GSw surface are able of water reduction. Nevertheless, no hydrogen evolution was observed during the photocatalytic experiment with GSw, which is probably due to quick electron-hole recombination.

Similarly, GSw-Pd does not shows any photocatalytic activity. According to the diagram of the Fig. 11a, the relative energy of the electrons excited from HOMO to LUMO of Pd clusters under light radiation is able of hydrogen reduction on the Pd cluster surface. Moreover, according to the literature data [58], the Gibbs energy of Pd-hydrogen interaction, should also favour water reduction to take place at Pd surface. Thus, probably the small amount of Pd and /or the quick recombination of electron-holes in Pd clusters determine the hydrogen formation is also negligible. On the other hand, the possible transference of the electrons from the LUMO of Pd clusters to the surface of GSw is probably reduced as the former are placed at the edges of both the sheets and defects of GSw, resulting in a poor contact of Pd and GSw surfaces, which makes the electron transference between these phases difficult.

In contrast with these results, the photocatalytic activity of the GSw-CdS hybrid significantly enhances that of the CdS by a factor of 7.5. According to Fig. 11a this result can be explained on the basis of an efficient transference of excited electrons in the CdS phase to the GSw surface which is favoured by the uniform distribution of the relatively small CdS nanoparticles in close contact with the graphene surface. It is worth comparing this result with that obtained in a previous work in which a hybrid (labelled G-Tren-CdS) based in CdS and an aromatic polyamine (labelled Tren)-functionalized graphene (G) was used [19]. Thus, when G-Tren-CdS is used the hydrogen production is 2.05 larger than that obtained with CdS, i.e. the GSw-CdS efficiency in water reduction outperforms that of G-Tren-CdS by a 3.7 factor. This difference, is probably due to the functionalization of G with Tren takes place via non-covalent attachment of the aromatic moiety of Tren to the Cπ centres of the graphene layers [19]. This fact significantly reduces the graphene surface available for reduction of H_3O^+ ions [19,34]. Nevertheless, in the case of GSw the functionalization with sulfur containing groups occurs at the edges and defects of the graphene layers which results in the graphene surface is preserved after functionalization.

The photocatalytic H_2 production with GSw-Pd-CdS outperforms that of GSw-CdS by a factor of c.a. 4.2. This large improvement of the catalytic performance points out to the important role of the Pd clusters as cocatalyst. Although it shouldnt be discarded that missimportant hydrogen reduction takes place on Pd surface (see above), the main role of Pd cocatalyst probably consists in a charge transference between the

Pd clusters and the CdS semiconductor, which favours the stabilization of the electron-hole pairs created in the latter under light radiation. The charge transference is favoured by the close contact between CdS and Pd phases of GSw-Pd-CdS (Fig. 6b). According to the electronic diagram in Fig. 11a the relative position of the valence band of CdS component and the E_{HOMO} of Pd clusters determines the possible hole transference from the former to the latter.

The photocatalytic water reduction when a Pd-CdS mixture is used results in 2.40 mmol h^{-1} g^{-1}, which is significantly larger than that of CdS but almost half of that obtained with GSw-Pd-CdS. This clearly points out to: i) the synergy between the CdS and Pd phases greatly favours the stabilization of the electron-hole pairs in CdS and ii) the important role of GSw surface which behaves as electron receptor for water reduction and favours a large dispersion of small CdS particles. TEM images of Pd NPs and Pd-CdS mixture together with the element distribution map of the last appear in Fig. S4b and c. It is seen a close contact of the CdS and Pd phases and that the size of the Pd and CdS NPs are larger than those in GSw-Pd-CdS (Fig. 6).

In summary the GSw-Pd-CdS photocatalyst shows excellent behavior that multiplies 31.1 times that of CdS which outperforms that of the analogous G-Tren-PdS-CdS [19]. In addition, its AQE (%) value almost doubles that of the homologous G-Tren-PdS-CdS [19]. The CdS component in the hybrid is in close contact with both the GSw surface and the Pd clusters. Nevertheless, the GSw and Pd clusters (which are at the edges and defects of the layers) do not have or have poor contact one to other, which probably limits the charge transference between them. According to the electronic diagram of Fig. 11a, the alignment of the CdS CB and the unoccupied orbitals of GSw facilitates the transference of the excited electrons from the former to the latter which allows H_2 formation on the surface of graphene. Moreover, the suitable alignment of the CdS VB and the Pd HOMO orbitals facilitates the hole transference from the CdS VB to the Pd HOMO orbitals. The photocatalytic reaction ends by the reduction of holes with the sacrificial agent, Na_2S / Na_2SO_3, resulting in the formation of $Na_2S_2O_3$.

Both G-Tren-PdS-CdS [19] and GSw-Pd-CdS have similar structures but the second shows a better catalytic performance which is mainly determined by: i) the mild treatment to functionalize the surface of G with sulfur containing groups by CS_2 plasma preserves most of the sp^2 moieties whose C-π sites play a key role in the reaction. Nevertheless, in G-Tren-PdS-CdS part of these sites are blocked due to the functionalization with Tren takes place via the interaction with Cπ centres [19]; ii) the high stability of the sulfur functions covalently bonded to the surface of GSw conditions the formation of very small (2– 3 nm) and size-uniform Pd clusters via attachment to these sulfur functions. This determines the high stability of the Pd clusters and the efficient light-harvesting in the whole UV-visible range. Moreover, the poor contact of Pd to GSw adds efficiency to the CdS-Pd hole transport. Finally, assuming that it should be expected that the lack of stacking in GSw remains after deposition of Pd and CdS, it could be hypothesized that this fact should also contribute to the excellent photocatalytic performance of GSw-Pd-CdS.

The photocatalytic activities of several CdS-based photocatalysts bearing carbon-derivatives and metals are shown in Table 1. As the experimental conditions vary (i.e. light source, atmospheric pressure vs closed gas circulation, sacrificial agent…) a reliable parameter to compare the photocatalyst efficiencies, is the enhanced factor in relation to CdS. It is seen that GSw-Pd-CdS exhibits a higher enhanced factor than the rest of photocatalysts based on graphene acting as support and having metal nanoparticles (Pd, PdS or Pt) as cocatalysts. This enhanced factor is significant and shows the potential application of this type of photocatalysts in the H_2 production. Moreover, the behavior of GSw-Pd-CdS points out that an important aspect in the design of this type of catalysts is to preserve as unaltered as possible the planar sp^2 moieties of graphene [59].

4. Conclusions

Functionalization of a few layer graphene, G [19,27] via cold CS_2 plasma treatment [21] provide an excellent graphene platform, GSw, with similar textural properties as G. GSw behaves as efficient support for CdS in photocatalytic water reduction. Preservation in GSw of the few layer graphene nature of G, allows efficient exposure of the particles of CdS photocatalyst to light. The S-functions are added to graphene through the reaction of CS_2 plasma with the graphene oxygen functions, which are mainly placed at the edges of the graphene sheets. This is an important point in the excellent photocatalytic performance of GSw-Pd-CdS due to Cπ centres act as reduction sites together to the surface of CdS. In addition, as the more the extension of sp^2 is preserved the smaller the sizes of deposited CdS nanoparticles, i.e. the larger the surface of the photocatalyst is exposed to the incident light. The deposition of Pd on the surface of graphene takes place via interaction of Pd (soft Lewis acid) with S (soft Lewis base). Pd is adsorbed in the photocatalyst as small clusters. The attachment of Pd to S-functions probably leads to the lack or the scarce contact of Pd with graphene sp^2 moieties which determines that the main role of Pd, which is the hole transport from CdS, is more efficient. These results encourage to get more insight into this point by studying the behavior of similar materials with different amounts of Pd clusters. Moreover, using other graphene supports with smaller layer surface area, i.e. graphene nanoplatelets, less prone to stacking than graphene also is probably beneficial to improve the quantum yield of this class of photocatalysts.

Author statement

The authors confirm that the manuscript has been read and approved by all named authors and that there are no other persons who satisfied the criteria for authorship but are not listed. The authors further confirm that the order of authors listed in the manuscript has been approved by all of them.

CRediT authorship contribution statement

María L. Godino-Salido: Conceptualization, Formal analysis, Investigation, Methodology, Writing – original draft, Writing – review & editing. **Alba M. Valbuena-Rus:** Formal analysis, Investigation, Methodology. **María D. Gutiérrez-Valero:** Investigation, Methodology. **Victor K. Abdelkader-Fernández:** Investigation, Methodology. **Rubén Cruz-Sánchez:** Investigation, Methodology. **F. Javier López-Garzón:** Validation, Writing – review & editing. **Manuel Melguizo:** Conceptualization, Validation. **Rafael López-Garzón:** Conceptualization, Writing

Table 1
Comparison of photocatalytic data of CdS-based photocatalysts bearing carbon-derivatives and metals.

Photocatalyst	Sacrificial Agent	Light source	Activity (mmol·h^{-1}·g^{-1})	Enhanced factor	Reference
G-WS_2/Pt/CdS (4.2 wt%/1wt%/94.8wt%)	Na_2S/Na_2SO_3	500 W Xe lamp (λ ≥ 420 nm)	1.842	c.a. 10	[60]
G-Nanoribbons/Pt/CdS (2wt%/1wt%/97wt%)	Lactic Acid	300 W Xe lamp (λ ≥ 400 nm)	1.891	3.7	[61]
3DGN/Pt/CdS (2wt%/1wt%/97wt%)	Na_2S/Na_2SO_3	300 W Xe lamp (λ ≥ 400 nm)	2.310	9.3	[62]
g-C_3N_4/Pd/CdS (15wt%/5wt%/80wt%)	Na_2S/Na_2SO_3	300 W Xe lamp (λ ≥ 420 nm)	0.293	12.0	[63]
G-Tren/PdS/CdS (5wt%/0.5wt%/94.5wt%)	Na_2S/Na_2SO_3	Simulated solar irradiation (AM 1.5 G)	2.30	18.9	[19]
GSw/Pd/CdS (4.5wt%/0.5wt%/95wt%)	Na_2S/Na_2SO_3	Simulated solar irradiation (AM 1.5 G)	3.79	31.1	This work

– original draft.

Declaration of competing interest

The authors declare that they have no known competing financial interests or personal relationships that could have appeared to influence the work reported in this paper.

Data availability

Data will be made available on request.

Acknowledgments

Support from the Spanish Government (Project RTI2018-101558-B-C21), the Autonomous Regional Government (Junta de Andalucía, Group PAIDI FQM273 and RNM342) and the University of Jaén (EI_FQM6-2023) is gratefully acknowledged. Technical and human support provided by SCAI of University of Jaén and CIC of University of Granada, and funding for open access charge provided by the University of Jaén / CBUA are also acknowledged.

Supplementary materials

Supplementary material associated with this article can be found, in the online version, at doi:10.1016/j.surfin.2024.104078.

References

[1] D. Gielen, F. Boshell, D. Saygin, M.D. Bazilian, N. Wagner, R. Gorini, The role of renewable energy in the global energy transformation, Energy Strateg. Rev. 24 (2019) 38–50, https://doi.org/10.1016/j.esr.2019.01.006.

[2] F. Manzano-Agugliaro, A. Alcayde, F.G. Montoya, A. Zapata-Sierra, C. Gil, Scientific production of renewable energies worldwide: an overview, Renew. Sustain. Energy Rev. 18 (2013) 134–143, https://doi.org/10.1016/J.RSER.2012.10.020.

[3] C. Jiang, S.J.A. Moniz, A. Wang, T. Zhang, J. Tang, Photoelectrochemical devices for solar water splitting-materials and challenges, Chem. Soc. Rev. 46 (2017) 4645, https://doi.org/10.1039/c6cs00306k.

[4] P. Wang, T. Wu, C. Wang, J. Hou, J. Qian, Y. Ao, Combining heterojunction engineering with surface cocatalyst modification to synergistically enhance the photocatalytic hydrogen evolution performance of cadmium sulfide nanorods, ACS Sustain. Chem. Eng. 5 (2017) 7670–7677, https://doi.org/10.1021/acssuschemeng.7b01043.

[5] K.A. Alzahrani, A.A. Ismail, α-Fe_2O_3/CeO_2 S-scheme heterojunction photocatalyst for enhanced photocatalytic H_2 evolution, Surf. Interface. 39 (2023) 102935, https://doi.org/10.1016/j.surfin.2023.102935.

[6] R.K. Chava, N. Son, Y.S. Kim, M. Kang, Integration of perovskite type Bi_2MoO_6 nanosheets onto one dimensional CdS: a type-II heterostructured photocatalytic system for efficient charge separation in the hydrogen evolution reaction, Inorg. Chem. Front. 7 (2020) 2818–2832, https://doi.org/10.1039/d0qi00339e.

[7] Q. Li, B. Guo, J. Yu, J. Ran, B. Zhang, H. Yan, J.R. Gong, Highly efficient visible-light-driven photocatalytic hydrogen production of CdS-cluster-decorated graphene nanosheets, J. Am. Chem. Soc. 133 (2011) 10878–10884, https://doi.org/10.1021/ja2025454.

[8] J. Xu, W. Zhong, D. Gao, X. Wang, P. Wang, H. Yu, Phosphorus-enriched platinum diphosphide nanodots as a highly efficient cocatalyst for photocatalytic H_2 evolution of CdS, Chem. Eng. J. 439 (2022) 135758, https://doi.org/10.1016/j.cej.2022.135758.

[9] Y. Chen, W. Zhong, F. Chen, P. Wang, J. Fan, H. Yu, Photoinduced self-stability mechanism of CdS photocatalyst: the dependence of photocorrosion and H_2-evolution performance, J. Mater. Sci. Technol. 121 (2022) 19–27, https://doi.org/10.1016/j.jmst.2021.12.051.

[10] M. Matsumura, S. Furukawa, Y. Sabo, H. Tsubomura, Cadmium sulfide photocatalyzed hydrogen production from aqueous solutions of sulfite: effect of crystal structure and preparation method of the catalyst, J. Phys. Chem. 89 (1985) 1327–1329, https://doi.org/10.1021/j100254a001.

[11] J.-F. Reber, M. Rusek, Photochemical hydrogen production with platinized suspensions of cadmium sulfide and cadmium zinc sulfide modified by silver sulfide, J. Phys. Chem. 90 (1986) 824–834, https://doi.org/10.1021/j100277a024.

[12] Y. Xu, W. Zhao, R. Xu, Y. Shi, B. Zhang, Synthesis of ultrathin CdS nanosheets as efficient visible-light-driven water splitting photocatalysts for hydrogen evolution, Chem. Commun. 49 (2013) 9803–9805, https://doi.org/10.1039/c3cc46342g.

[13] C. Bie, J. Fu, B. Cheng, L. Zhang, Ultrathin CdS nanosheets with tunable thickness and efficient photocatalytic hydrogen generation, Appl. Surf. Sci. 462 (2018) 606–614, https://doi.org/10.1016/j.apsusc.2018.08.130.

[14] S. Kouser, A. Thannikoth, U. Gupta, U.V. Waghmare, C.N.R. Rao, 2D-GaS as a photocatalyst for water splitting to produce H_2, Small 11 (2015) 4723–4730, https://doi.org/10.1002/smll.201501077.

[15] R. Patil, Y. Khollam, A. Kadam, B. Bond, R. Potdar, B. Nadekar, U.T. Nakate, S. F. Shiakh, P.S. More, Ultrasonic spray deposited CdS-GO composite films for solar cell applications, Surf. Interface. 42 (2023) 103331, https://doi.org/10.1016/j.surfin.2023.103331.

[16] A. Chernikov, T.C. Berkelbach, H.M. Hill, A. Rigosi, Y. Li, O.B. Aslan, D. R. Reichman, M.S. Hybertsen, T.F. Heinz, Exciton binding energy and nonhydrogenic Rydberg series in monolayer WS_2, Phys. Rev. Lett. 113 (2014) 076802, https://doi.org/10.1103/PhysRevLett.113.076802.

[17] S. Ma, J. Xie, J. Wen, K. He, X. Li, W. Liu, X. Zhang, Constructing 2D layered hybrid CdS nanosheets/MoS_2 heterojunctions for enhanced visible-light photocatalytic H_2 generation, Appl. Surf. Sci. 391 (2017) 580–591, https://doi.org/10.1016/j.apsusc.2016.07.067.

[18] H. Li, J. Pan, W. Zhao, C. Li, The 2D nickel-molybdenum bimetals sulfide synergistic modified hollow cubic CdS towards enhanced photocatalytic water splitting hydrogen production, Appl. Surf. Sci. 497 (2019) 143769, https://doi.org/10.1016/j.apsusc.2019.143769.

[19] A.M. Valbuena-Rus, M.D. Gutiérrez-Valero, P. Arranz-Mascarós, R. López-Garzón, M. Melguizo, J. Vernet-García, M. Pérez-Mendoza, M.L. Godino-Salido, Synergy of semiconductor components of non-covalent functionalized (PdS doped)-G CdS NPs composite provide efficient photocatalytic water reduction under visible light, Appl. Surf. Sci. 554 (2021) 149646, https://doi.org/10.1016/J.APSUSC.2021.149646.

[20] M. Savastano, P. Arranz-Mascarós, M.P. Clares, R. Cuesta, M.L. Godino-Salido, L. Guijarro, M.D. Gutiérrez-Valero, M. Inclán, A. Bianchi, E. García-España, R. López-Garzón, A new heterogeneous catalyst obtained via supramolecular decoration of graphene with a Pd^{2+} azamacrocyclic complex, Molecules 24 (2019) 2714, https://doi.org/10.3390/molecules24152714.

[21] V.K. Abdelkader-Fernández, M. Domingo-García, F.J. López-Garzón, D. M. Fernandes, C. Freire, M.D. López de la Torre, M. Melguizo, M.L. Godino-Salido, M. Pérez-Mendoza, Expanding graphene properties by a simple S-doping methodology based on cold CS_2 plasma, Carbon N Y 144 (2019) 269–279, https://doi.org/10.1016/j.carbon.2018.12.045.

[22] A.M. Valbuena-Rus, M. Savastano, P. Arranz-Mascarós, C. Bazzicalupi, M.P. Clares, M.L. Godino-Salido, M.D. Gutiérrez-Valero, M. Inclán, A. Bianchi, E. García-España, R. López-Garzón, Noncovalent assembly and catalytic activity of hybrid materials based on Pd complexes adsorbed on multiwalled carbon nanotubes, graphene, and graphene nanoplatelets, Inorg Chem. 61 (2022) 12610–12624, https://doi.org/10.1021/acs.inorgchem.2c01559.

[23] E. Gracia-Espino, G. Hu, A. Shchukarev, T. Wå, Understanding the interface of six-shell cuboctahedral and icosahedral palladium clusters on reduced graphene oxide: experimental and theoretical study, J. Am. Chem. Soc. 136 (2014) 6626–6633, https://doi.org/10.1021/ja412259h.

[24] C. Premi, N. Jain, A nitrogen and sulphur functionalized graphene oxide-palladium nanoparticle hybrid catalyst for an efficient Heck coupling, RSC Adv. 6 (2016) 74961–74967, https://doi.org/10.1039/c6ra09996c.

[25] X. Xing, A. Hermann, X. Kuang, M. Ju, C. Lu, Y. Jin, X. Xia, G. Maroulis, Insights into the geometries, electronic and magnetic properties of neutral and charged palladium clusters, Sci. Rep. 6 (2016) 19656, https://doi.org/10.1038/srep19656.

[26] L. Wei, X. Yao, X. Tian, M. Cao, W. Chen, Y. She, S. Zhang, A DFT investigation of the effects of doped Pb atoms on Pdn clusters ($13 \leqslant n \leqslant 116$), Comput. Theor. Chem. 966 (2011) 375–382, https://doi.org/10.1016/J.COMPTC.2011.03.041.

[27] P. Arranz-Mascarós, M.L. Godino-Salido, R. López-Garzón, C. García-Gallarín, I. Chamorro-Mena, F.J. López-Garzón, E. Fernández-García, M.D. Gutiérrez-Valero, Non-covalent functionalization of graphene to tune its band gap and stabilize metal nanoparticles on its surface, ACS Omega 5 (2020) 18849–18861, https://doi.org/10.1021/acsomega.0c02006.

[28] T.J. Bandosz, J. Jagiello, C. Contescu, J.A. Schwarz, Characterization of the surfaces of activated carbons in terms of their acidity constant distributions, Carbon N Y 31 (1993) 1193–1202, https://doi.org/10.1016/0008-6223(93)90072-I.

[29] J. Jagiełło, T.J. Bandosz, J.A. Schwarz, Carbon surface characterization in terms of its acidity constant distribution, Carbon N Y 32 (1994) 1026–1028, https://doi.org/10.1016/0008-6223(94)90066-3.

[30] P. Arranz, A. Bianchi, R. Cuesta, C. Giorgi, M.L. Godino, M.D. Gutiérrez, R. López, A. Santiago, Binding and removal of sulfate, phosphate, arsenate, tetrachloromercurate, and chromate in aqueous solution by means of an activated carbon functionalized with a pyrimidine-based anion receptor (HL). Crystal structures of $[H_3L(HgCl_4)]H_2O$ and $[H_3L(HgBr_4)]H_2O$ showing anion-π interactions, Inorg. Chem. 49 (2010) 9321–9332, https://doi.org/10.1021/ic100929f.

[31] T.-F. Yeh, J.-M. Syu, C. Cheng, T.-H. Chang, H. Teng, Graphite oxide as a photocatalyst for hydrogen production from water, Adv. Funct. Mater. 20 (2010) 2255–2262, https://doi.org/10.1002/adfm.201000274.

[32] H.J. Kuhn, S.E. Braslavsky, R. Schmidt, Chemical actinometry (IUPAC technical report), Pure Appl. Chem. 76 (2004) 2105–2146, https://doi.org/10.1351/pac200476122105.

[33] A. Braun, M.T. Maurette, E. Oliveros, Technologie Photochimique, Presses Polytechniques et Universitaires Romandes (PPUR), 1986.

[34] C. Leon y Leon, J. Solar, V. Calemma, L. Radovic, Evidence for the protonation of basal plane sites on carbon, Carbon N Y 30 (1992) 797–811, https://doi.org/10.1016/0008-6223(92)90164-R.
[35] G. Eda, Y.Y. Lin, C. Mattevi, H. Yamaguchi, H.A. Chen, I.S. Chen, C.W. Chen, M. Chhowalla, Blue photoluminescence from chemically derived graphene oxide, Adv. Mater. 22 (2010) 505–509, https://doi.org/10.1002/adma.200901996.
[36] Q. Lai, S. Zhu, X. Luo, M. Zou, S. Huang, Ultraviolet-visible spectroscopy of graphene oxides, AIP Adv. 2 (2012) 032146, https://doi.org/10.1063/1.4747817.
[37] B. Liu, W. Yu, Z. Yan, C. Tang, P. Gu, J. Chen, Z. Liu, Z. Huang, Broadband, wide-angle, and polarization-insensitive enhancement of light absorption in monolayer graphene over whole visible spectrum, Result. Phys. 18 (2020), https://doi.org/10.1016/J.RINP.2020.103134.
[38] T. Yoon, Q. Wu, D.J. Yun, S.H. Kim, Y.J. Song, Direct tuning of graphene work function via chemical vapor deposition control, Sci. Rep. 10 (2020) 1–6, https://doi.org/10.1038/s41598-020-66893-y.
[39] W. Rasband, Image J. (2015). https://imagej.nih.gov/ij/.
[40] W. Chamorro-Coral, A. Caillard, P. Brault, P. Andreazza, C. Coutanceau, S. Baranton, The role of oxygen on the growth of palladium clusters synthesized by gas aggregation source, Plasma Process. Polym. 16 (2019) e1900006, https://doi.org/10.1002/PPAP.201900006.
[41] N.V. Vorob'ev-Desyatovskii, S.A. Kubyshkin, R.I. Ibragimova, V.V. Kaichev, Y. A. Dubrovskii, V.N. Babakov, D.A. Pichugina, Study of sorption of platinum and palladium cyanometallate complexes as the key to understanding the mechanism of binding the $[Au(CN)_2]^-$ anion with carbon adsorbents, Russ. J. Gen. Chem. 82 (2012) 384–397, https://doi.org/10.1134/S107036321203005X.
[42] T. Tuntulani, G. Musie, J.H. Reibenspies, M.Y. Darensbourg, Metallosulfoxides and -sulfones: sulfur oxygenates of [l,5-Bis(2-mercaptoethyl)-l,5-diazacyclooctanato] palladium(II), Inorg. Chem. 34 (1995) 6279–6286, https://doi.org/10.1021/ic00129a012.
[43] G. Sipos, E.E. Drinkel, R. Dorta, The emergence of sulfoxides as efficient ligands in transition metal catalysis, Chem. Soc. Rev. 44 (2015) 3834–3860, https://doi.org/10.1039/c4cs00524d.
[44] J.H. Price, A.N. Williamson, R.F. Schramm, B.B. Wayland, Palladium(II) and platinum(II) alkyl sulfoxide complexes. Examples of sulfur-bonded, mixed sulfur- and oxygen-bonded, and totally oxygen-bonded complexes, Inorg. Chem. 11 (1972) 1280–1284, https://doi.org/10.1021/ic50112a025.
[45] A.V. Naumkin, A. Kraut-Vass, S.W. Gaarenstroom, C.J. Powell, N.I.S.T. X-ray, Photoelectron spectroscopy database. NIST standard reference database 20, version 4.1, Meas. Serv. Div. Natl. Inst. Stand. Technol (2012), https://doi.org/10.18434/T4T88K.
[46] T.-J. Wang, F.-M. Li, H. Huang, S.-W. Yin, P. Chen, P.-J. Jin, Y. Chen, Porous Pd-PdO Nanotubes for Methanol Electrooxidation, Adv. Funct. Mater. 30 (2020) 2000534, https://doi.org/10.1002/adfm.202000534.
[47] S. De Marchi, S. Núñez-Sánchez, G. Bodelón, J. Pérez-Juste and I. Pastoriza-Santos, Pd nanoparticles as a plasmonic material: synthesis, optical properties and applications, Nanoscale. 12 (2020) 23424–23443. https://doi.org/10.1039/d0nr06270g.
[48] Y.T. Kim, T. Mitani, Surface thiolation of carbon nanotubes as supports: a promising route for the high dispersion of Pt nanoparticles for electrocatalysts, J. Catal. 238 (2006) 394–401, https://doi.org/10.1016/j.jcat.2005.12.020.
[49] G.-W. Yang, G.-Y. Gao, G.-Y. Zhao, H.-L. Li, Effective adhesion of Pt nanoparticles on thiolated multi-walled carbon nanotubes and their use for fabricating electrocatalysts, Carbon N Y 45 (2007) 3036–3041, https://doi.org/10.1016/j.carbon.2007.06.021.
[50] H. Peng, J. Yong, H. Wang, Y. Gou, F. Wang, X. Zheng, Dual CdS–CoS/S,N-doped TiO_2 nanofibers for efficient visible-light induced H_2 evolution, Int. J. Hydrog. Energy 47 (2022) 31269–31278, https://doi.org/10.1016/j.ijhydene.2022.07.054.
[51] Y.J. Yuan, D. Chen, Z.T. Yu, Z.G. Zou, Cadmium sulfide-based nanomaterials for photocatalytic hydrogen production, J. Mater. Chem. A. 6 (2018) 11606–11630, https://doi.org/10.1039/c8ta00671g.
[52] S. Shenoy, E. Jang, T.J. Park, C.S. Gopinath, K. Sridharan, Cadmium sulfide nanostructures: influence of morphology on the photocatalytic degradation of erioglaucine and hydrogen generation, Appl. Surf. Sci. 483 (2019) 696–705, https://doi.org/10.1016/j.apsusc.2019.04.018.
[53] J. Riga, P. Snauwaert, A. De Pryck, R. Lazzaroni, J.P. Boutique, J.J. Verbist, J. L. Brédas, J.M. André, C. Taliani, Electronic structure of sulphur-containing conducting polymers, Synth. Met. 21 (1987) 223–228, https://doi.org/10.1016/0379-6779(87)90090-7.
[54] D.M. Poirier, J.H. Weaver, CdS by XPS, Surf. Sci. Spectra 2 (1993) 249–255, https://doi.org/10.1116/1.1247706.
[55] X. Chen, L. Liu, P.Y. Yu, S.S. Mao, Increasing solar absorption for photocatalysis with black hydrogenated titanium dioxide nanocrystals, Science 331 (2011) 746–750.
[56] J. Song, Y. Chen, D. Sun, X. Li, Perylenetetracarboxylic diimide modified $Zn_{0.7}Cd_{0.3}S$ hybrid photocatalyst for efficient hydrogen production from water under visible light irradiation, Inorg. Chem. Commun. 92 (2018) 27–34, https://doi.org/10.1016/j.inoche.2018.03.018.
[57] M. Mousavi, A. Habibi-Yangjeh, M. Abitorabi, Fabrication of novel magnetically separable nanocomposites using graphitic carbon nitride, silver phosphate and silver chloride and their applications in photocatalytic removal of different pollutants using visible-light irradiation, J. Colloid Interface Sci. 480 (2016) 218–231, https://doi.org/10.1016/J.JCIS.2016.07.021.
[58] J. Wang, H. Zhang, X. Wang, Recent methods for the synthesis of noble-metal-free hydrogen-evolution electrocatalysts: from nanoscale to sub-nanoscale, Small Method. 1 (2017) 1700118.
[59] M.Q. Yang, N. Zhang, M. Pagliaro, Y.J. Xu, Artificial photosynthesis over graphene-semiconductor composites. Are we getting better? Chem. Soc. Rev. 43 (2014) 8240–8254, https://doi.org/10.1039/c4cs00213j.
[60] Q. Xiang, F. Cheng, D. Lang, Hierarchical layered WS_2/graphene-modified CdS nanorods for efficient photocatalytic hydrogen evolution, ChemSusChem 9 (2016) 996–1002, https://doi.org/10.1002/CSSC.201501702.
[61] Y. Xia, B. Cheng, J. Fan, J. Yu, G. Liu, Y. Xia, B. Cheng, J.G. Yu, J.J. Fan, G. Liu, Unraveling photoexcited charge transfer pathway and process of CdS/graphene nanoribbon composites toward visible-light photocatalytic hydrogen evolution, Small 15 (2019) 1902459, https://doi.org/10.1002/SMLL.201902459.
[62] Z. Wang, Z. Liu, J. Chen, H. Yang, J. Luo, J. Gao, J. Zhang, C. Yang, S. Jia, B. Liu, Self-assembly of three-dimensional CdS nanosphere/graphene networks for efficient photocatalytic hydrogen evolution, J. Energy Chem. 31 (2019) 34–48, https://doi.org/10.1016/j.jechem.2018.05.006.
[63] N. Güy, Directional transfer of photocarriers on CdS/g-C_3N_4 heterojunction modified with Pd as a cocatalyst for synergistically enhanced photocatalytic hydrogen production, Appl. Surf. Sci. 522 (2020) 146442, https://doi.org/10.1016/J.APSUSC.2020.146442.